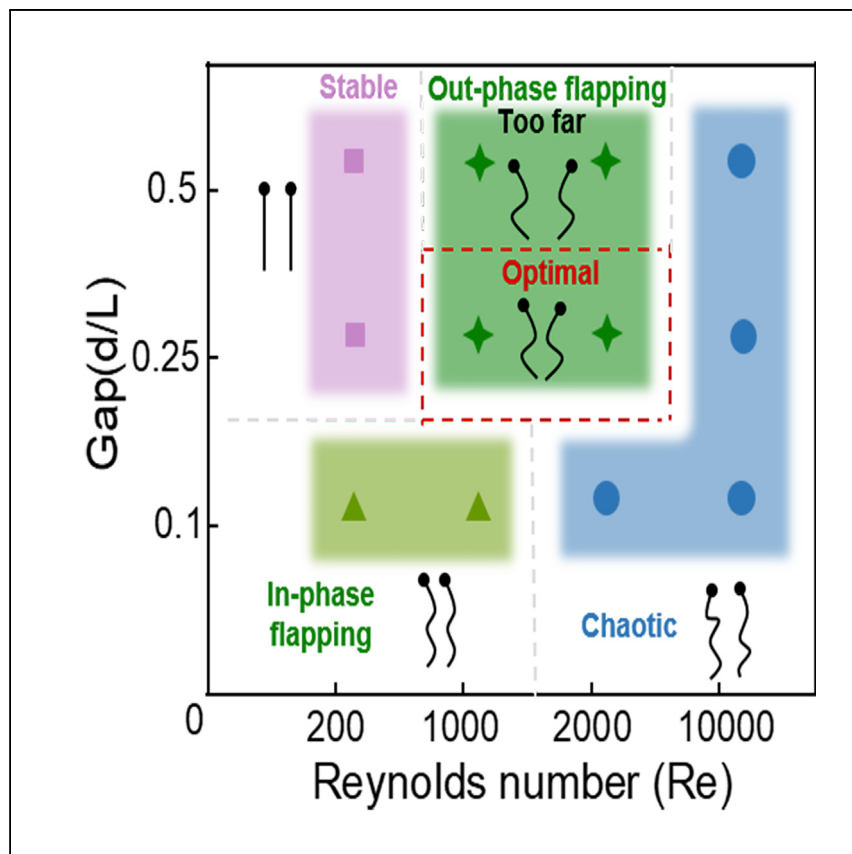


Article

# A Triboelectric Nanogenerator Exploiting the Bernoulli Effect for Scavenging Wind Energy



A triboelectric nanogenerator exploiting the Bernoulli effect for effectively scavenging wind energy is reported by Chen et al. The device operates at a low enabled flutter wind velocity of  $1.6 \text{ ms}^{-1}$  and a high conversion efficiency of 3.23%. The prospective wind harvester is a path to scavenge wind energy and can power some electronic devices in outdoor environments.

Xin Chen, Xingchen Ma, Weiwei Ren, ..., Xiaoqing Zhang, Xiaojing Mu, Ya Yang

x.zhang@tongji.edu.cn (X.Z.)  
mxjacj@cqu.edu.cn (X.M.)  
yayang@binn.cas.cn (Y.Y.)

## HIGHLIGHTS

A triboelectric nanogenerator exploiting the Bernoulli effect for wind harvesting

The B-TENG works with low flutter wind velocity and high conversion efficiency

The B-TENG can scavenge wind in any direction in an outdoor environment



Article

# A Triboelectric Nanogenerator Exploiting the Bernoulli Effect for Scavenging Wind Energy

Xin Chen,<sup>1,2,7</sup> Xingchen Ma,<sup>3,7</sup> Weiwei Ren,<sup>4,7</sup> Lingxiao Gao,<sup>1,2</sup> Shan Lu,<sup>1</sup> Daqiao Tong,<sup>1</sup> Fayang Wang,<sup>1</sup> Yu Chen,<sup>1</sup> Yi Huang,<sup>5</sup> Hao He,<sup>5</sup> Baoping Tang,<sup>5</sup> Jiajia Zhang,<sup>6</sup> Xiaoqing Zhang,<sup>3,\*</sup> Xiaojing Mu,<sup>1,\*</sup> and Ya Yang<sup>2,8,\*</sup>

## SUMMARY

Wind energy is one of the most cost-effective energy sources available today. Some techniques have been developed to scavenge wind energy, but making use of lower flutter velocity while maintaining high conversion efficiency remains challenging. Here, we report a triboelectric nanogenerator composed of two interacting triboelectric films with four flapping modes, enabling an effective work wind velocity as low as  $1.6 \text{ ms}^{-1}$  and a high conversion efficiency of 3.23%, which, to our knowledge, are better than previously reported values of wind energy scavenging. The output performance of B-TENG can be determined by device size and flow velocity; the optimized device exhibits an output voltage, current, and power of 175 V, 43  $\mu\text{A}$ , and 2.5 mW, respectively, with dimensions of  $3 \times 8 \times 2 \text{ cm}^3$  at a flow velocity of  $8 \text{ ms}^{-1}$ . The B-TENG may pave the way for future wind scavenging devices for a range of point-of-use applications.

## INTRODUCTION

Energy harvesting is the process of collecting energy from the surrounding environment and converting it into electricity, and it is gaining interest as a future next-generation energy source. Conventionally, electricity is supplied by a power plant or a battery, with the subsequent demands of electrical infrastructure or replacement of batteries. In recent years, the idea of using ambient energy in the forms of light, vibration, heat, radio waves, etc. has become increasingly attractive, and several methods to generate electricity from these different kinds of energy sources have been developed.<sup>1–3</sup> Wind power is one of the most cost-effective, lowest-priced energy sources available today.<sup>4–7</sup> Normally, wind turbines, the devices that convert wind energy into electrical energy, are used to harvest wind energy and are widely used in our daily life. However, the high cost basis, resulting noise, and aesthetic pollution are still issues.<sup>8–11</sup> Thus, most research groups have focused on piezoelectric nanogenerators to convert mechanical energy into electricity based on the piezoelectric effect.<sup>12–16</sup> Chen et al.<sup>17</sup> and Sun et al.<sup>17</sup> designed the micro piezoelectric nanogenerator, which uses vortex flutter effects. The design overcame the drawback of the traditional piezoelectric nanogenerator, which uses single-frequency acquisition, but the output power remains low.<sup>17,18</sup> The recently invented triboelectric nanogenerator is a promising approach to harvest ambient energy and convert it into electrical energy based on triboelectric and electrostatic effects, given its low cost, light weight, and high power density,<sup>19–34</sup> and there has been much research in this field. Other groups reported triboelectric nanogenerators for scavenging wind energy based on vortex fluttering and designed a self-powered wind vector

<sup>1</sup>Key Laboratory of Optoelectronic Technology & Systems Ministry of Education, International R&D Center of Micro-nano Systems and New Materials Technology, Chongqing University, Chongqing 400044, China

<sup>2</sup>CAS Center for Excellence in Nanoscience, Beijing Key Laboratory of Micro-nano Energy and Sensors, Beijing Institute of Nanoenergy and Nanosystems, Chinese Academy of Sciences, Beijing 100083, China

<sup>3</sup>Shanghai Key Laboratory of Special Artificial Microstructure Materials and Technology, School of Physics Science and Engineering, Tongji University, Shanghai 200092, China

<sup>4</sup>Infineon Technologies Asia Pacific Pte. Ltd., Singapore, Singapore

<sup>5</sup>State Key Laboratory of Mechanical Transmission, Chongqing University, Chongqing 400044, China

<sup>6</sup>Chongqing University of Posts and Telecommunications, Chongqing 400044, China

<sup>7</sup>These authors contributed equally

<sup>8</sup>Lead Contact

\*Correspondence: [x.zhang@tongji.edu.cn](mailto:x.zhang@tongji.edu.cn) (X.Z.), [mxjac@cqu.edu.cn](mailto:mxjac@cqu.edu.cn) (X.M.), [yang@binn.cas.cn](mailto:yang@binn.cas.cn) (Y.Y.)

<https://doi.org/10.1016/j.xcrp.2020.100207>



sensor.<sup>35–42</sup> Bae et al.<sup>43</sup> investigated the coupled interaction between a fluttering flexible flag and a rigid plate, and the flutter-driven triboelectric generator exhibited high electrical performance at a high frequency of 158 Hz. This research explored fluidics mechanisms combined with the triboelectric nanogenerators, but there are still some issues to be explored, such as working with a low wind flutter velocity, lowering the resonant frequency at which the triboelectric nano-generator works, and increasing the mechanical-to-electrical conversion efficiency.

Previously research has been performed on the basic dynamics of two coupled flexible structures, such as flags, flapping in the air: the Bernoulli effect. The first experimental study of two flexible filament interactions as a model for flags in two-dimensional wind was performed by Zhang et al.,<sup>44</sup> and the experimental result shows that, if the inter-filament distance  $d$  is sufficiently small ( $d/L < 0.21 \pm 0.04$ ), then the two filaments tend to phase lock and flap in phase with each other. As the distance increases ( $d/L > 0.21$ ), the filaments switch to be locked out of phase, with the flap symmetrically about the center line. As  $d$  increases further, the coupling between the two filaments weakens, and each tends to behave independent of the other. In addition, the interaction of the two thin films placed in parallel directions has so far received scant attention, although their coupled dynamics can be a very powerful vibration source for triboelectric generators because of the self-sustained nature. Previous studies have shown that the fluttering wind velocity of the two films is lower than that of a single film, which would be more practical in reality.

The triboelectric nanogenerator based on the Bernoulli effect is proposed to solve these issues. We first investigated the dynamics of the fluid-flexible structure interaction of two films to obtain the stable flapping boundaries of fluttering. The dynamics of this structure can be classified into four states: stable (no contact), out-of-phase flapping, in-phase flapping, and chaotic. The dynamics of out-of-phase flapping are utilized to develop a Bernoulli effect-dominated triboelectric nanogenerator (B-TENG) composed of a ferroelectric polyvinylidene fluoride (PVDF) film with an Ag electrode and a PVDF film coated with fluorinated polyethylene propylene (FEP), which are placed in parallel with the stream flow, based on knowledge of the interaction dynamics between the two thin films. The results show that the optimized output voltage, current, and power for a  $3 \times 8 \text{ cm}^2$  B-TENG can reach 175 V, 43  $\mu\text{A}$ , and 2.5 mW, respectively, at an input flow velocity of  $8 \text{ ms}^{-1}$ . In addition, the device was demonstrated to be capable of charging and sensing; 100 light emitting diodes (LEDs) in series were illuminated, and a self-powered thermometer was realized. Moreover, a 100- $\mu\text{F}$  capacitor was charged to 3 V within 3 min at an incoming air flow velocity of  $8 \text{ ms}^{-1}$ . Thus, self-powered pressure monitoring of a pipeline system was achieved through one very-low-cost and lightweight device. The proposed B-TENG may solve the issues of the high flow velocity requirements with efficient scavenging and the low output power in recent investigations and provide a new mechanism for harvesting wind energy with high efficiency.

## RESULTS

### Analysis of the Bernoulli Effect Formed by the Two Interacting Films

The Bernoulli effect is a statement of the relationship between flow speed and pressure in a fluid system. In essence, when the speed of horizontal flow through a fluid increases, the pressure decreases. When air flows between the films, the flow velocity between the two films is increased and the pressure is decreased, forming the Bernoulli effect. To ensure feasibility of the B-TENG from the Bernoulli effect dominating the two films' interaction, it is vital to analyze the detailed dynamic

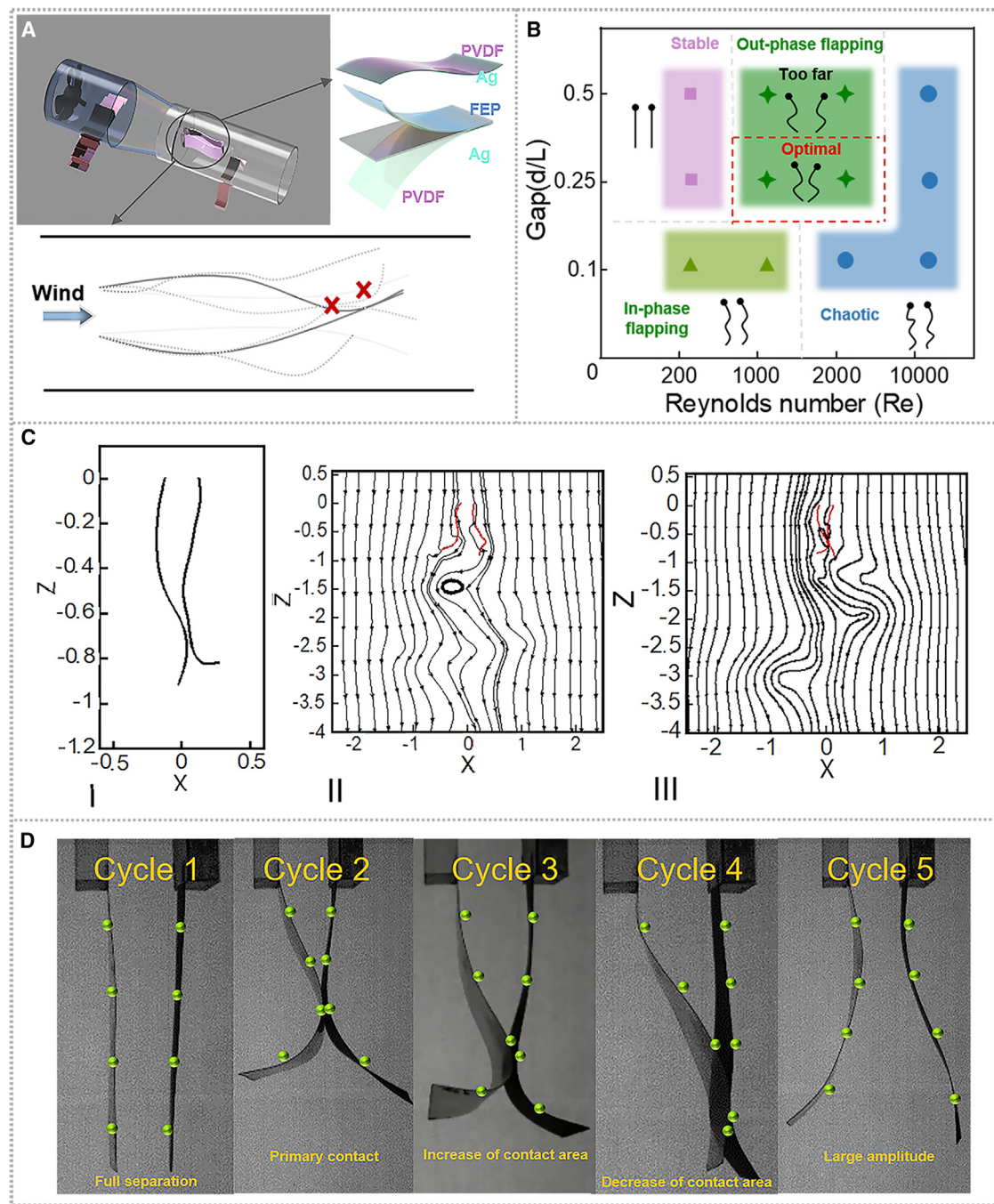


**Figure 1. The Bernoulli Effect Applied to Wind Energy Harvesting**

(A) The system of wind harvesting and construction of the B-TENG.

(B) The fluttering mode of the triboelectric nanogenerator.

(C) Simulation of the out-of-phase flapping mode of two interaction films.

(D) The out-of-phase flapping behavior of the structure of two interaction films with dimensions of  $8(L) \times 3(w)$  was captured by a high-speed camera under a wind velocity of  $8\text{ ms}^{-1}$ . The green fluorescent bulbs in the picture were used to identify the trajectory of two flapping films.

characteristics of the Bernoulli effect generated by the two interaction films. The wind harvesting system is displayed in Figure 1A. A flexible PVDF film was deposited with silver nanoparticles coupling with another FEP-attached PVDF film face to face

in parallel directions. Upon steady air flow, the two interaction films forming the Bernoulli effect exhibited dynamic behavior as rapid periodic contact and separation; the trajectory of this is depicted in [Figure 1B](#). The interaction of two films flapping with a node, the oscillation amplitude is tiny from the fixed end to the node. Below the node, one film held by the law a traveling wave propagated toward the trailing edge with increasing amplitude, and the interaction of two films present the fluttering state of flapping as the Bernoulli effect. Thus, our work simulated through immersed boundary-lattice Boltzmann method via the method of computational fluid dynamics (CFD) based on the previous work. The theory to accumulate the boundary condition of the Bernoulli effect forming with two interaction films in an incompressible flow is depicted as follows. Here we present the two interaction films as the line mass, and the incompressible viscous fluid flow is described using the Navier-Stokes and continuity equations,

$$\rho \left( \frac{\partial \vec{u}}{\partial t} + \vec{u} \cdot \nabla \vec{u} \right) = -\nabla p + \mu \Delta \vec{u} + \vec{f}, \quad (\text{Equation 1})$$

$$\nabla \cdot \vec{u} = 0, \quad (\text{Equation 2})$$

where  $\vec{u}$  is the fluid velocity,  $p$  is the fluid pressure,  $\mu$  is the dynamic viscosity of the fluid, and  $\vec{f}$  is the external force field. The geometrically nonlinear equation of motion for the filament is

$$\rho_s \frac{\partial^2 \vec{X}}{\partial t^2} - \frac{\partial}{\partial s} \left[ T(s) \frac{\partial \vec{X}}{\partial s} \right] + K_b \frac{\partial^4 \vec{X}}{\partial s^4} = \vec{F}, \quad (\text{Equation 3})$$

with the tensile stress

$$T(s) = K_s \left( \left( \frac{\partial \vec{X}}{\partial s} \cdot \frac{\partial \vec{X}}{\partial s} \right)^{1/2} - 1 \right), \quad (\text{Equation 4})$$

where  $\rho_s$  is the linear density of the filament,  $s$  is the Lagrangian coordinate along the length,  $K_s$  is the stretching coefficient,  $K_b$  is the flexure modulus,  $\vec{X}$  is the Lagrangian point of the filament, and  $\vec{F}$  is the external force on the Lagrangian points.

Using the immersed boundary method, the relation of the external force density on the filament and the external force density on flow field can be expressed by

$$\vec{f}(\vec{x}, t) = - \int \vec{F}(\vec{X}(s, t), t) \delta(-\vec{X}(s, t)) ds, \quad (\text{Equation 5})$$

where  $\delta(\cdot)$  is the nondimensional Dirac delta function.

Nondimensionalizing the mass density  $\rho_s$ , flexure modulus  $K_b$ , and stretching coefficient  $K_s$  by the characteristic length  $L$ , velocity  $U$ , and fluid density  $\rho_f$ , we obtain

$$M = \frac{\rho_s}{\rho_f L}, \hat{K}_s = \frac{K_s}{\rho_f U^2 L}, \hat{K}_b = \frac{K_b}{\rho_f U^2 L^3}. \quad (\text{Equation 6})$$

Based on these theories, the simulation parameters are displayed in [Table S1](#). Because the FEP is too thin compared with the thickness of PVDF, and to simplify the calculation of flutter progress, we just calculated the movement of basement (PVDF). [45–51](#) From the above formulas, the stiffness and size of the hybrid films are the key consideration for the motion mode of two interaction films. Thus, with an inter-filament distance 0.1, 0.25, and 0.5, three cases under different wind velocities at the above boundary conditions were used to explore the motion modes of two interaction films. Based on our numerical results, for the small inter-filament distance of 0.1, the two films move in phase at the lower wind speed, and the two films move

chaotically at a higher velocity. When the displacement of the two filaments increases to  $d/L = 0.25$ , the two filaments flap in an out-of-phase model as a stable state, as depicted in [Video S1](#); the equilibrium state would be broken at a higher velocity and enter the chaotic state. As the inter-film distance increases to 0.5, the two films move out of phase, but two films are not in contact and also move chaotically at a higher wind speed; it is not possible to form a triboelectric nanogenerator under this condition. These numerical computations ignore the gravity of the film; the simulation results are depicted in [Figure S1](#). Based on the former facts, the mode of displacement of the two films at  $d/L = 0.25$  was chosen to construct the triboelectric nanogenerator for a follow-up study, and the numerical simulation results of this mode are diagrammed in [Figure 1C](#). The results show the vortex state of the air flow as the two films move in the out-of-phase model. In addition, a high-speed video camera was utilized to record the kinetics mode of the two films in the out-of-phase state at a wind velocity of  $8 \text{ ms}^{-1}$ , as shown in [Figure 1D](#). The two films were in stable mode when there was no wind or breeze in cycle 1. As the flow velocity increased, the films moved out of phase and formed the triboelectric nanogenerator possessing two contacts, as depicted in the cycle 2, cycle 3, and cycle 4. Then the films were in a separate state (cycle 5) for the next loop contact, and the motion mode was recorded ([Video S2](#)). Whereas as the wind velocity increase to a certain extent, the motion of the two films became chaotic ([Video S3](#)). The experimental flapping mode of the two films was in accordance with the numeral simulation, confirming the accuracy of the size of the film and interface in the simulation.

### B-TENG Setup

The construction of the triboelectric nanogenerator based on the model of the Bernoulli effect and the parameters of the B-TENG were calculated according to the simulation of the two flapping films mode. As depicted in [Figure 1A](#), the B-TENG was composed of an Ag electrode and laminated triboelectric film, forming the B-TENG with vertical contact separation mode.<sup>52–54</sup> The ferroelectric PVDF was chosen as the substrate for the B-TENG because of the hardness of the film presenting the two flapping films mode and ferroelectric material properties that could enhance the electric energy output of triboelectric nanogenerators. The Ag electrode was fabricated by vacuum evaporation method on a PVDF flexible substrate. To obtain the excellent electric energy output of the nanogenerator, a laminated triboelectric film was investigated, which was composed of a FEP film and a PVDF film. The electrostatic bonding approach was applied to laminate the FEP and PVDF layers. [Figure 2A](#) illustrates the preparation process for the FEP-PVDF compound system. First, the FEP film was exposed to a corona with a tip voltage of  $-15 \text{ kV}$  for 5 min. Thereafter, a PVDF film was attached to the charged surface of the FEP film and absorbed by electrostatic effect. Finally, a second corona, charging with the same parameters as the first, was applied to the bonded FEP-PVDF system. In the actual application, delamination may happen to the electrostatic laminated hybrid films. One solution may be thermal sealing around the four sides of the laminated films, which can be done using a plastic packaging machine. Just four sides are because the PVDF will return a polarity at a high temperature. Then the charge storage stability of the compound system was tested through surface potential decay with an electrostatic voltmeter, as depicted in [Figure S2](#). Multiple points on each sample were measured, and an average value was calculated. To investigate the charge storage stability in the lab environment, samples were stored at room temperature for 8 days, and the surface potential was measured, as depicted in [Figure 2B](#). The results show that the surface potential of the laminated films decayed quickly on the first day, and then the decay tended to be flat, proving that the laminated films possess favorable charge storage stability. Additionally, the reliability of the laminated films was tested

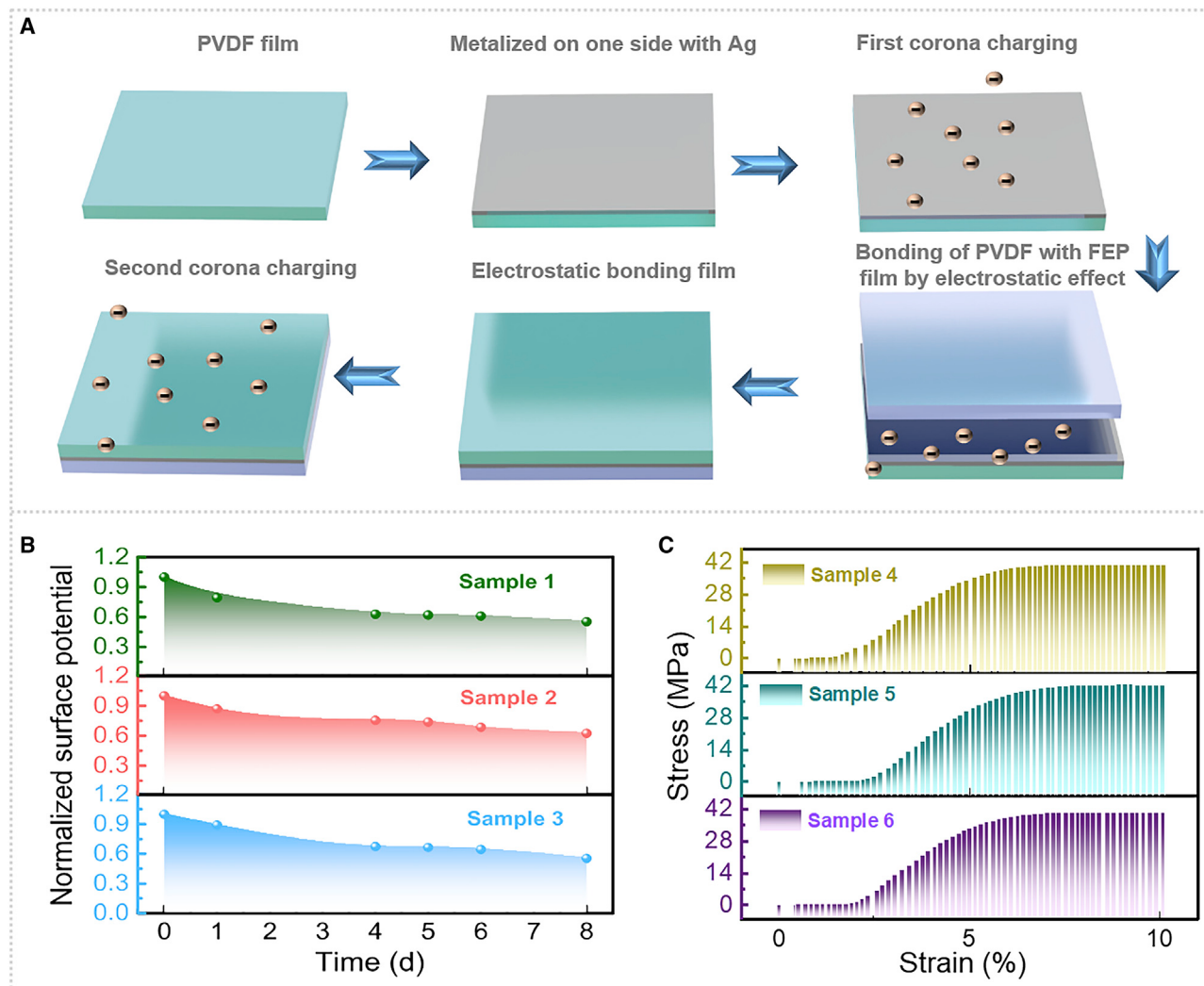


**Figure 2. Fabrication of the High-Performance Triboelectric Nanogenerator**

(A) The technological fabrication process of the high-performance laminated film.

(B) The charge stability of the laminated film.

(C) The reliability of the laminated triboelectric film.

utilized a tensile tester in controlled velocity mode at a speed of 30 mm/min, and the results shown in Figure 2C indicate that the laminated films are advantageous for wind energy harvesting under normal environmental conditions.

#### Working Principle and Electric Characteristics of the B-TENG

The output electricity generation process of B-TENG is realized by the sequence of contact-propagation-separation motion induced by the two interacting triboelectric films flapping. Actually, the output power will be highly related to the contact area, and the maximum contact area was designed using the CFD simulation. Considering the  $K_b$  and  $K_s$  of the film, the maximum contact area of two films was at out-of-phase flapping at  $d/L = 0.25$ , and the primary contact happened at the 1/3 position of the upper part of the membrane. Furthermore, the generation process of the B-TENG was simulated using the COMSOL 5.3a software according to the flapping behavior diagrammed in Figure 1D. A schematic showing the electric potential and the working principle of the B-TENG is shown in Figure 3A; the electricity output of the B-

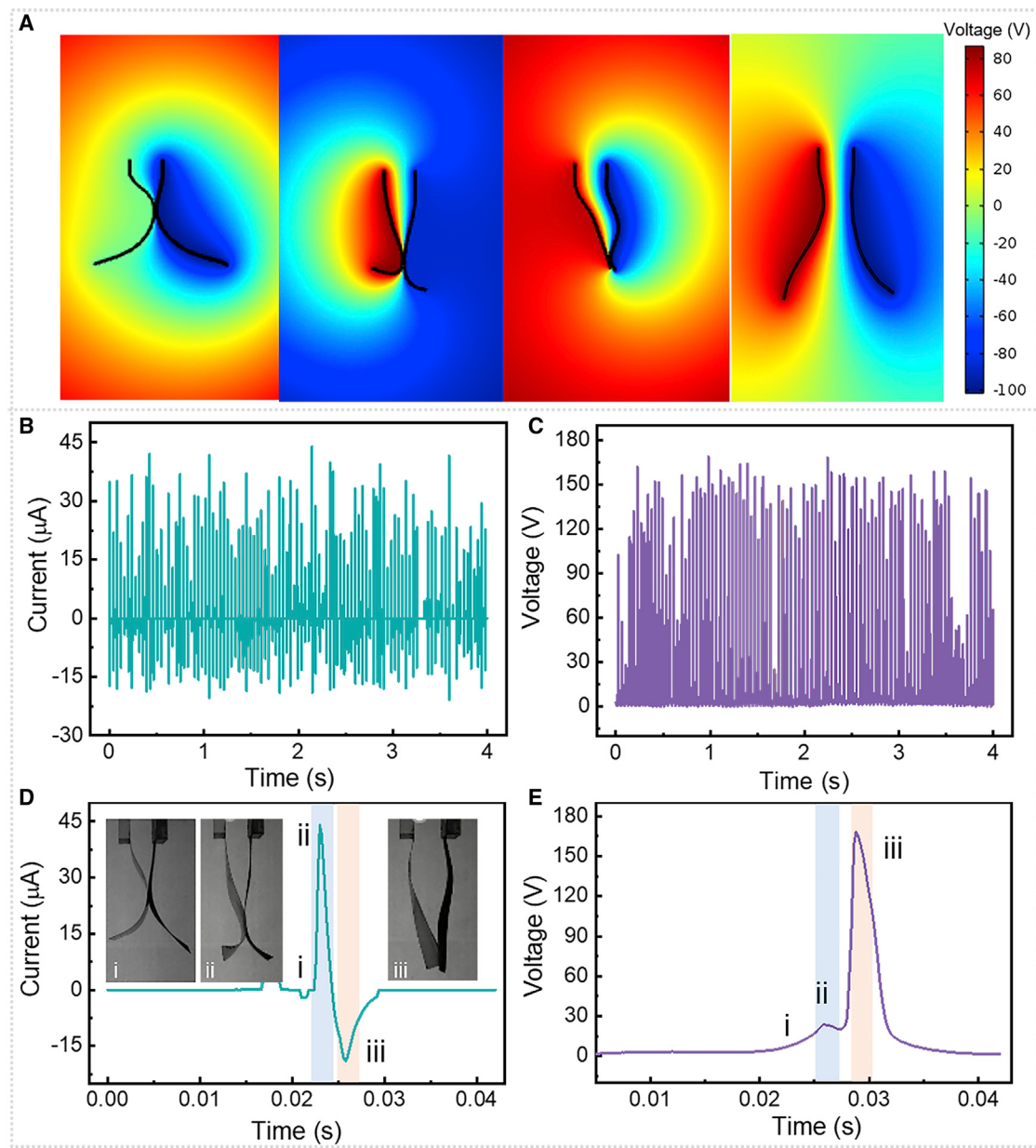


**Figure 3. The Working Principle of the Wind Triboelectric Nanogenerator**

(A) The working principle of the nanogenerator simulated by the COMOSOL 5.3a software.

(B) The output current of the triboelectric nanogenerator.

(C) The output voltage of the wind triboelectric nanogenerator.

(D and E) The output electric characteristics of the wind triboelectric nanogenerator. (i) The mode of primary contact. (ii) The mode for increasing the contact area. (iii) The mode for decreasing the contact area.

TENG was produced by the gradual increase and decrease of the total contact area of the triboelectric film via wave propagation. The B-TENG is based on the metal insulator module; the FEP used as the normal polarity insulator material could gain electrons on its surface, and the surface could be charged negatively by rubbing the metal surface. When the two films were blown by the wind, the films presented out-of-phase flapping, and the surface charge density increased, but there was no electric potential difference at the time of the first contact. After the contact,

the propagation process occurred, and that brought about a gradual increase and decrease in contact surface area, sequentially. That is to say, the gradual increase in contact surface area caused a higher electric potential on the triboelectric films, and the gradual decrease in surface area induced a decline in electric potential on the triboelectric films. When the two films periodically contacted each other, a regularly alternating current was generated because of the difference in the two triboelectric films.

To investigate the electric characteristics of the B-TENG possessing the unique fluid mechanism, the output voltage and current were measured with an electrometer for the out-of-phase flapping mode under a flow velocity of  $8\text{ ms}^{-1}$  at a size of  $3 \times 8\text{ cm}^2$ . In the mode of out-of-phase flapping, transferred charges produced an alternating current output with a short-circuit current of  $43\text{ }\mu\text{A}$  and an output voltage of  $175\text{ V}$ . Compared with the common materials utilized in the triboelectric nanogenerator, the electret possesses higher output electricity, as illustrated in [Figures 3A](#) and [3B](#) and [Figure S3](#). Analyzing the portrait of signal output waveform and the flapping mode of the two interaction films, we found that the films' interaction includes the following steps: a primary contact of the curved area ([Figures 3D-i](#) and [E-i](#)), an increase in contact area ([Figures 3D-ii](#) and [E-ii](#)), a decrease in contact area ([Figures 3D-iii](#) and [E-iii](#)), and complete separation. The output characteristics were greatly restricted in the kinstate module of the B-TENG. In conclusion, the electricity output of the B-TENG is determined by the effective contact area and the rate of triboelectric charge separation. Thus, deeply investigating the flapping mode of the two interaction triboelectric films at different flow velocities is critical.

### Output Performance and Durability of the B-TENG

To study the relationship between the electricity output and wind velocity, a systematic measurement was designed using wind velocities varying from  $4\text{ ms}^{-1}$  to  $15\text{ ms}^{-1}$ ; the result is depicted in [Figures 4A](#) and [4B](#). To clarify, the flutter velocity of the B-TENG is about  $1.6\text{ ms}^{-1}$ , and the test results are depicted in [Figure S4](#) and [Video S4](#). The short-circuit current of the B-TENG at a flow velocity of  $4\text{ ms}^{-1}$  was  $15\text{ }\mu\text{A}$ . With an increase in wind velocity, the peak value of short-circuit current increases because a higher wind speed results in more transferred charge, as discussed before, and a higher charge transfer rate with an increase in contact frequency, as shown in [Figure 4B](#). The current of the B-TENG reached a maximum of  $43\text{ }\mu\text{A}$  at a wind velocity of  $8\text{ ms}^{-1}$ , and then the value decreased as the wind velocity increased. The variation tendency of the output voltage had the same trend; the output voltage was  $115\text{ V}$  at a velocity of  $4\text{ ms}^{-1}$ , reached a maximum voltage of  $175\text{ V}$  at a velocity of  $8\text{ ms}^{-1}$ , and then decreased at a flow velocity of more than  $8\text{ ms}^{-1}$ . The reason for this phenomenon could be the efficient change in surface contact area during flapping with an increase in flow velocity. The fluttering mode of the B-TENG was out-of-phase flapping with the wind velocity varying from  $4\text{ ms}^{-1}$  to  $8\text{ ms}^{-1}$ , a variation of the higher fluttering speed was due to the increase in the contact force which induced higher electricity output during this stage. As the wind velocity increased, the fluttering motion became chaotic, and irregular fluttering could also be observed that unpredictably decreased the effective contact area, which is the reason for the lower electricity output. The movement frequency of B-TENG was also calculated through MATLAB 2015b using arithmetics of fast Fourier transformation (FFT); the results are shown in [Figure 4C](#). The results showed that the movement frequency of B-TENG increased as the wind velocity increased from  $4\text{ ms}^{-1}$  to  $15\text{ ms}^{-1}$ , a vital element of the increase in electricity output. Although the output was lower at the high wind velocity than at the low velocity, a higher average output power was obtained. Subsequently, the peak output power of

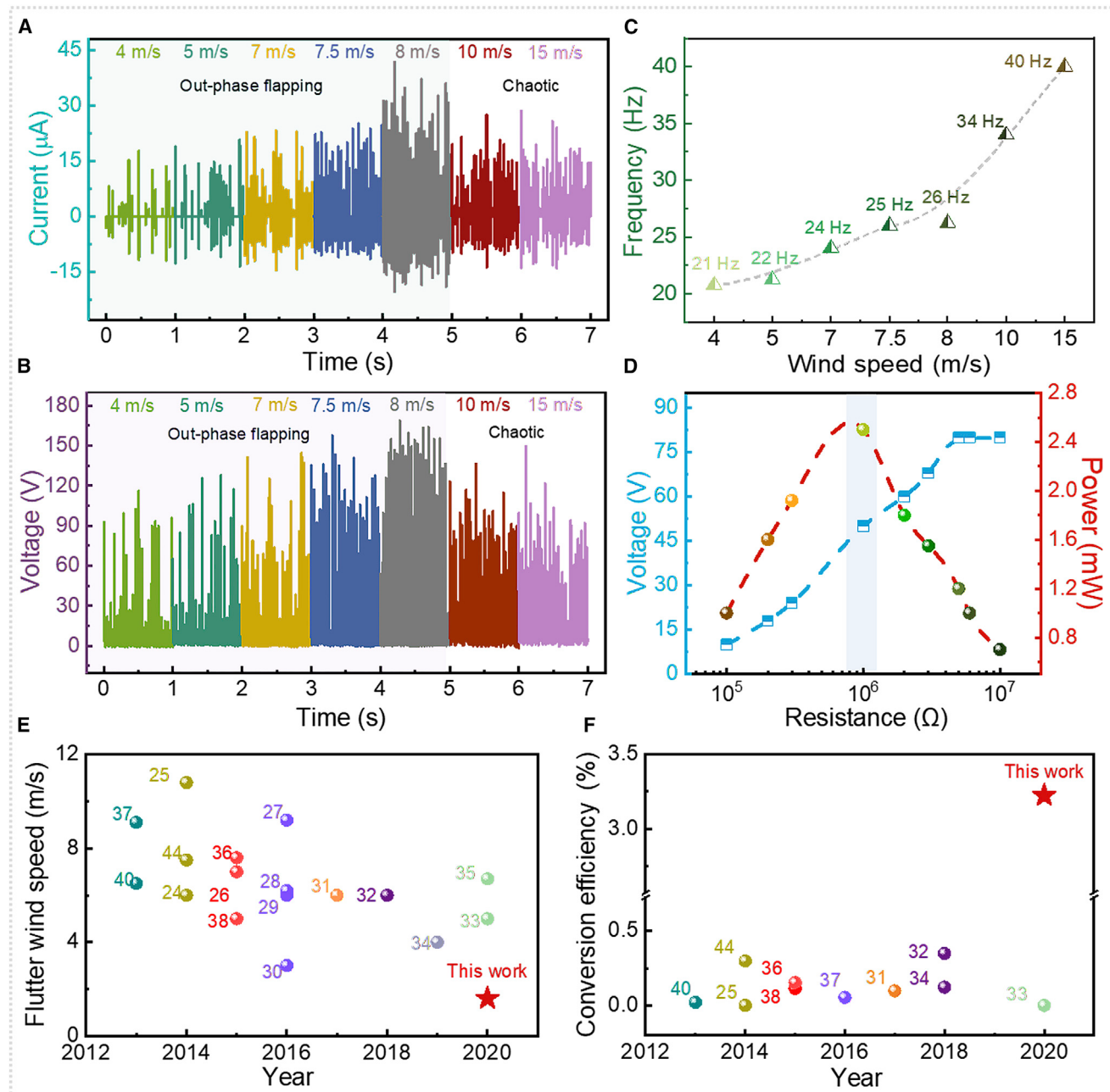


**Figure 4. The Output Performance of the Wind Triboelectric Nanogenerator with Different Flow Velocities**

- (A) The output current of the triboelectric nanogenerator with different flow velocities.
- (B) The output voltage of the triboelectric nanogenerator with different flow velocities.
- (C) The motion frequency of the triboelectric nanogenerator with different flow velocities.
- (D) The output power of the triboelectric nanogenerator.
- (E) Comparison of the lowest enabled flutter wind speed in this work and previous values.
- (F) Comparison of the conversion efficiency in this work and previous work.

the B-TENG was measured. When a variable external load was connected to the B-TENG, the output voltage rose as the load resistance increased. The instantaneous peak output power of the B-TENG increased from 0.8 mW to 2.5 mW as the resistance changed from 100 k $\Omega$  to 1 M $\Omega$  and then decreased with the larger load

resistance, which indicated that the maximum instantaneous peak output power was at a resistance of  $1\text{ M}\Omega$ , as depicted in the Figure 4D, and the average output power was about  $73\text{ }\mu\text{W}$ . We compared this with previous work about triboelectric nanogenerators for wind energy harvesting, where the flutter wind velocities were recorded. Compared with the initially enabled flutter wind velocity of most previous work, the initially enabled flutter wind velocity in our work is  $1.6\text{ ms}^{-1}$ , which is in the vanguard of triboelectric nanogenerators for wind energy scavenging because of the particular fluidics design (Figure 4E). This unique feature accelerates practical applications of the wind triboelectric nanogenerator. The electromechanical conversion effect can be calculated as follows:<sup>55</sup>

$$Q_V = v \cdot S, \quad (\text{Equation 7})$$

where  $Q_V$  is the volume flow,  $v$  is the wind velocity, and  $S$  is the air outlet area;

$$Q_m = Q_V \cdot \rho, \quad (\text{Equation 8})$$

where  $Q_m$  is the mass flow rate and  $\rho$  is air density;

$$P_o = \frac{V^2}{R}, \text{ and} \quad (\text{Equation 9})$$

$$P_I = \frac{Q_m \cdot v^2}{2}, \text{ and} \quad (\text{Equation 10})$$

$$\eta = \frac{P_o}{P_I} \times 100\%, \quad (\text{Equation 11})$$

where  $P_o$  is the instantaneous output power,  $V$  is the load voltage,  $R$  is the load,  $P_I$  is the instantaneous input power, and  $\eta$  is the conversion efficiency. The  $\eta$  of previous studies was less than 1% because the flutter wind velocities in most of the reported work were over  $10\text{ ms}^{-1}$ , and the instantaneous input power was significantly more than the output power. In our work, the  $\eta$  of the B-TENG is about 3.23% at a wind velocity of  $6\text{ ms}^{-1}$ , which is much larger than the previously reported values, as displayed in Figure 4F. In addition, the durability of the B-TENG was investigated, and the result is depicted in Figure S5. The tests reveal that the B-TENG has good reliability and stability. Furthermore, the practicability of the TENG was studied. The device was designed as  $5\text{ (w)} \times 20\text{ (L)} \times 5\text{ (H) cm}^3$  under breezy condition, as illustrated in Figure 5A and Figure S6, proving that the B-TENG can be used in an outdoor environment (Video S5).

### Application of the B-TENG

The electric output capability of the B-TENG was investigated in follow-up experiments. The charging ability of the B-TENG was investigated, and a capacitance from  $10\text{--}100\text{ }\mu\text{F}$  was chosen as the representative capacitor experimental target; the charging curve of these capacitors is presented in Figure S7. The results showed that the smaller the capacitance ( $10\text{ }\mu\text{F}$ ) of the capacitor, the shorter the charging time (10 s) to achieve the target, whereas the larger capacitance ( $100\text{ }\mu\text{F}$ ) necessitated a longer charging time (180 s). Then, because the B-TENG had excellent electrical output, about 100 LEDs were connected in series and lighted by the B-TENG; the results are shown in Figure S8 and Video S6. Furthermore, a self-powered low-power temperature sensor node was realized, as demonstrated in Figure S9. Also, the external excitation of the above experimental was a wind velocity at  $8\text{ ms}^{-1}$ ; the experiment is shown in Video S7.

In addition, a self-powered monitoring system of pipe pressure was constructed (Figure 5C). The system consists of the B-TENG, energy management circuits, and wireless transmission modules. The function of the B-TENG is to monitor the flow pressure in the pipe (Figure 5D). The rectifier bridge and electrolytic capacitor ( $690\text{ }\mu\text{F}$ ) were used to

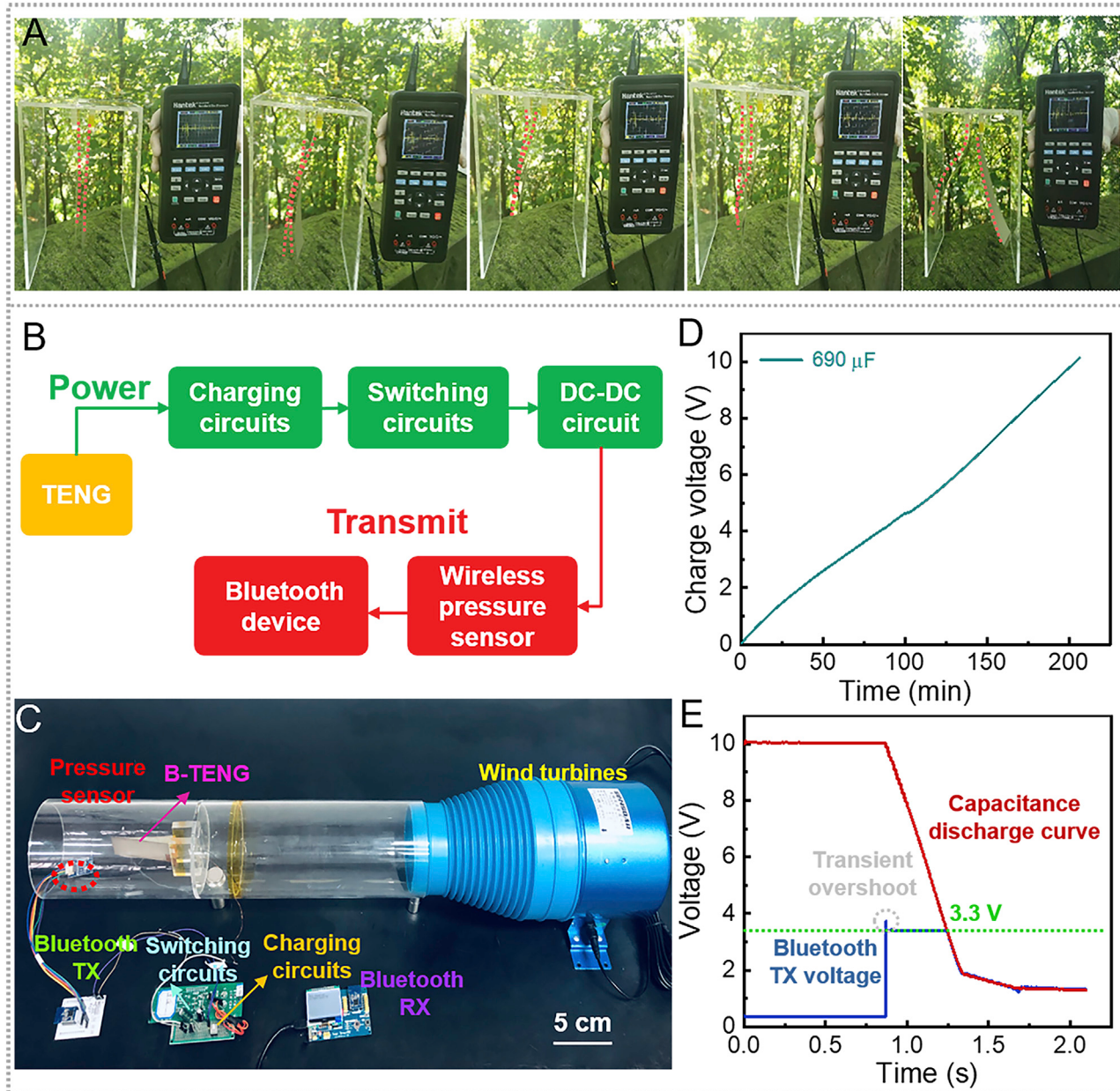


**Figure 5. The Electric Capability of the Triboelectric Nanogenerator**

- (A) The practicality of the B-TENG in an outdoor environment.
- (B) The mechanism of the self-powered pipe pressure monitoring system.
- (C) The picture of the self-powered pressure sensing system.
- (D) The charging curve of the self-powered system.
- (E) The discharge curve of the self-powered system.

store the energy generated while the B-TENG started to generate electricity, and the transistor, diode, and N-channel metal-oxide-semiconductor field-effect transistor (MOSFET) together with low dropout regulator (LDO, MAX 666) constituted the switching circuits to control the time of capacity discharge for powering the wireless nodes sensing transmission. The power calculated for sending pressure sensor data is 12.4 mJ, and according to the numeration, the voltage of the capacity was set to 10 V (Figure 5E), whereas the energy stored from this process is about 34.5 mJ, enough for

sending once, as shown in [Figure 5F](#). Although the power supply output voltage exceeds its setting, the hardware switches on, and the discharge power of the capacitor power is connected to the voltage regulator module LDO, regulating the voltage to 3.3 V to power the wireless sensing nodes (there is a transient overshoot as power on). The wireless sensing node system consists of a pressure sensor, a Bluetooth module transmitter, a Bluetooth receiver, and a low-power liquid crystal display (LCD). The air pressure sensor communicates with Bluetooth through inter-integrated circuit ( $I^2C$ ). After obtaining the current pipe pressure, the pressure signal is broadcast to the receiving end through the Bluetooth radio frequency module. The receiver scans the broadcast packet, and the pressure signal is decoded and displayed in the LCD; this is shown in [Video S8](#). The results of the above experiments indicate that the B-TENG has excellent output performance.

## DISCUSSION

In summary, we have demonstrated that Bernoulli effect-based flapping behavior can be utilized to induce contact-propagation-separation of two interaction films for wind energy scavenging. The dynamic interactions include stable, out-of-phase flapping, in-phase flapping, and chaotic modes induced by different device sizes and wind velocities. The simulations and experiments indicate that out-of-phase flapping results in higher output performance. By increasing the wind velocity, the output performance of the wind harvester can be increased, reaching a maximum value at a wind velocity of  $8\text{ ms}^{-1}$ , including a voltage of 175 V, a current of 43  $\mu\text{A}$ , and an output power of 2.5 mW. The output performance of the device is associated with the factors of contact force, effective contact area, and contact motion type, including stable periodic contact and chaotic contact. The fabricated B-TENG exhibits a low enabled flutter velocity of  $1.6\text{ ms}^{-1}$  and a high conversion efficiency of 3.23%, which are much better than those of all previously reported values in the wind scavenging field. Moreover, the B-TENG can light 100 LEDs, a self-powered thermometer, and a self-powered pipe pressure sensing system. This work introduces a new mechanism of utilizing B-TENGs for wind energy scavenging; the designed device has excellent electrical performance with the potential to power small electric devices.

## EXPERIMENTAL PROCEDURES

### Resource Availability

#### Lead Contact

Further information and requests for resources should be directed to and will be fulfilled by the Lead Contact, Ya Yang ([yayang@binn.cas.cn](mailto:yayang@binn.cas.cn)).

#### Materials Availability

This study did not generate new unique reagents.

#### Data and Code Availability

All of the key data supporting the findings of this study are presented within the article and the [Supplemental Information](#). All other data are available from the Lead Contact upon reasonable request.

### Fabrication of the B-TENG

The B-TENG is composed of triboelectric laminated films and Ag electrodes  $3(w) \times 8(L)$  cm in size and separated by 2 cm, and the air outlet size is  $2 \times 5\text{ cm}^2$ . The triboelectric laminated film includes the PVDF film (110  $\mu\text{m}$ ) and FEP film (25  $\mu\text{m}$ ), combined by electrostatic adsorption, and the process of electrostatic adsorption was achieved using a high-precision, high-voltage power module (DW-P303-1AC). The Ag electrodes (6  $\mu\text{m}$ ) were coated on the PVDF film through electronic printing technology.

### Measurement System

The charge storage stability of the laminated film was measured by an electrostatic voltmeter (Trek 370) with a compensation method, and the reliability of the film was tested by a tensile tester (KJ-1065A). The output electricity (output voltage, short-circuit current) of the B-TENG was measured using a programmable electrometer (Keithley 6514) and a data acquisition card (NIPCI-6259) on a desktop personal computer (PC). In addition, external excitation was generated by a variable-frequency wind fan (SE-150), and the output electricity of the B-TENG was measured at different wind velocities using this wind fan system.

### Wireless Pipeline Monitoring System

The wireless sensing node system is composed of a barometric pressure sensor (BMP388), Bluetooth TX (CC2541), and Bluetooth RX(CC2541). The pressure sensor converted the perceived pressure analog signal into a digital signal and transmitted it through Bluetooth to the remote transmitter. The digital signal was processed by the microcontroller unit (MCU) in the data-sending module, transmitted to the data-receiving end, and displayed on the LCD screen.

## SUPPLEMENTAL INFORMATION

Supplemental Information can be found online at <https://doi.org/10.1016/j.xcrp.2020.100207>.

## ACKNOWLEDGMENTS

This work was supported by the National Key Research and Development Program of China (2019YFB2004800), the Fundamental Research Funds for the Central Universities (2019CDCGGD320), the Chongqing University Scientific Research Reserve Top Talent Cultivation Program, the Defense Key Disciplines Lab of Novel Micro-nano Devices and Systems Technology, the External Cooperation Program of BIC (CQU2019HBRC1A04), the Chinese Academy of Sciences (121411KYS820150028), the 2015 Annual Beijing Talents Fund (2015000021223ZK32), the Qingdao National Laboratory for Marine Science and Technology (2017ASKJ01), and the University of the Chinese Academy of Sciences (Y8540XX2D2). The authors also gratefully acknowledge financial support from the Natural Science Foundation of China (NSFC; 61761136004) and the Graduate Scientific Research and Innovation Foundation of Chongqing, China.

## AUTHOR CONTRIBUTIONS

X.Z., X.M., and Y.Y. conceived the idea and guided the project. X.C. and L.G. fabricated the devices and performed measurements. X.C., X.M., and L.G. discussed the experimental results, drew figures, and prepared the manuscript. S.L. and D.T. designed the energy management circuits and self-powered systems. All authors contributed to data analysis and commented on the manuscript.

## DECLARATION OF INTERESTS

The authors declare no competing interests.

Received: July 6, 2020

Revised: August 10, 2020

Accepted: August 21, 2020

Published: September 23, 2020

## REFERENCES

1. Beeby, S.P., and O'Donnell, T. (2009). Energy Harvesting Technologies (Springer).
2. Sudevalayam, S., and Kulkarni, P. (2011). Energy harvesting sensor nodes: survey and implications. *IEEE Comm. Surv. and Tutor.* 13, 443–461.
3. Alhwari, M., Mohammad, B., Saleh, H., and Ismail, M. (2018). Energy harvesting for self-powered wearable devices (Springer).
4. Burton, T., Jenkins, N., Sharpe, D., and Bossanyi, E. (2001). Wind energy handbook (Wiley).
5. Kuvlesky, W.P., Jr., Brennan, L.A., Morrison, M.L., Boydston, K.K., Ballard, B.M., and Bryant, F.C. (2007). Wind Energy Development and Wildlife Conservation: Challenges and Opportunities. *J. Wildl. Manage.* 71, 2487–2498.
6. Munteanu, I., Cutululis, N.A., Bratu, A.I., and Ceanga, E. (2005). Optimization of variable speed wind power systems based on a LQG approach. *Control Eng. Pract.* 13, 903.
7. Alberto, T.B., Álvaro, A., and Dorronsoro, J.R. (2017). Regression tree ensembles for wind energy and solar radiation prediction. *Neurocomputing* 31, 151–156.
8. Khaligh, A., and Onar, O. (2009). Energy harvesting: Solar, wind, and ocean energy conversion systems (CRC Press).
9. Muller, S., Deicke, M., and De Doncker, R.W. (2002). Doubly fed induction generator systems for wind turbines. *IEEE Ind. Appl. Mag.* 8, 26.
10. Hameed, Z., Hong, Y.S., Cho, Y.M., Ahn, S.H., and Song, C.K. (2009). Condition monitoring and fault detection of wind turbines and related algorithms: a review. *Renew. Sustain. Energy Rev.* 13, 1–39.
11. Aza-Gnandji, M.R., Fifatin, F.X., Dubas, F., Nounangnonhou, T.C., and Vianou, A. (2019). Investigation on offshore wind energy potential in benin republic. *Wind Eng. Published online September 9, 2019. <https://doi.org/10.1177/0309524X19872768>.*
12. Li, S., Yuan, J., and Lipson, H. (2011). Ambient wind energy harvesting using cross-flow fluttering. *J. Appl. Physiol.* 109, 026104.
13. Sun, D., Xu, Y., Chen, H., Wu, K., Liu, K., and Yu, Y. (2012). A mean flow acoustic engine capable of wind energy harvesting. *Energy Convers. Manage.* 63, 101.
14. De Maequ, C., and Erturk, A. (2013). Electroaeroelastic analysis of airfoil-based wind energy harvesting using piezoelectric transduction and electromagnetic induction. *J. Intel. Mat. Syst. Str.* 24, 846–854.
15. Zhao, L., and Yang, Y. (2018). An impact-based broadband aeroelastic energy harvester for concurrent wind and base vibration energy harvesting. *Appl. Energy* 212, 233.
16. Zhou, M., Chen, Q., Xu, Z., and Wang, W. (2019). Piezoelectric wind energy harvesting device based on the inverted cantilever beam with leaf-inspired extensions. *AIP Adv.* 9, 035213.
17. Chen, Y., Mu, X., Wang, T., Ren, W., Yang, Y., Wang, Z.L., Sun, C., and Gu, A.Y. (2016). Flutter phenomenon in flow driven energy harvester—A unified theoretical model for "stiff" and "flexible" materials. *Sci. Rep.* 6, 35180.
18. Sun, C.L., Mu, X.J., Siow, L.Y., Tsang, W.M., Ji, H., Chang, H.K., Zhang, Q., Gu, Q.Y., and Kwong, D.L. (2014). A miniaturization strategy for harvesting vibration energy utilizing helmholtz resonance and vortex shedding effect. *IEEE Electr. Device L.* 35, 271–273.
19. Gao, L., Hu, D., Qi, M., Gong, J., Zhou, H., Chen, X., Chen, J., Cai, J., Wu, L., Hu, N., et al. (2018). A double-helix-structured triboelectric nanogenerator enhanced with positive charge traps for self-powered temperature sensing and smart-home control systems. *Nanoscale* 10, 19781–19790.
20. Chen, X., Gao, L., Lu, S., Chen, J., Zhou, H., Wang, T., Wang, A., Zhang, Z., Guo, S., Mu, X., et al. (2020). A chaotic pendulum triboelectric-electromagnetic hybridized nanogenerator for wave. *Nano Energy* 69, 104440.
21. Lu, S., Gao, L., Chen, X., Tong, D., Yuan, P., Mu, X., and Yu, H. (2020). Stimultaneous energy harvesting and signal sensing from a single triboelectric nanogenerator for intelligent self-powered wireless sensing system. *Nano Energy* 75, 104813.
22. Gao, L., Chen, X., Lu, S., Zhou, H., Xie, W., Chen, J., Qi, M., Yu, H., Mu, X., Wang, Z.L., and Yang, Y. (2019). Enhancing the output performance of triboelectric nanogenerator via grating-electrode-enabled surface plasmon excitation. *Adv. Energy Mater.* 44, 1902725.
23. Gao, L., Lu, S., Xie, W., Chen, X., Wu, L., Wang, T., Wang, A., Yue, C., Tong, D., Lei, W., et al. (2020). A self-powered and self-functional tracking system based on triboelectro-electromagnetic hybridized blue energy harvesting module. *Nano Energy* 72, 104684.
24. Meng, X.S., Zhu, G., and Wang, Z.L. (2014). Robust thin-film generator based on segmented contact-electrification for harvesting wind energy. *ACS Appl. Mater. Interfaces* 6, 8011–8016.
25. Guo, H., He, X., Zhong, J., Zhong, Q., Leng, Q., Hu, C., Chen, J., Tian, L., Xi, Y., and Zhou, J. (2014). A nanogenerator for harvesting airflow energy and light energy. *J. Mater. Chem. A* 2, 2079–2087.
26. Chen, S., Gao, C., Tang, W., Zhu, H., Han, Y., Jiang, Q., Li, T., Cao, X., and Wang, Z.L. (2015). Self-powered cleaning of air pollution by wind driven triboelectric nanogenerator. *Nano Energy* 14, 217.
27. Quan, Z., Han, C.B., Jiang, T., and Wang, Z.L. (2016). Robust Thin Films-Based Triboelectric Nanogenerator Arrays for Harvesting Bidirectional Wind Energy. *Adv. Energy Mater.* 6, 1501799.
28. Zhang, L., Zhang, B., Chen, J., Jin, L., Deng, W., Tang, J., Zhang, H., Pan, H., Zhu, M., Yang, W., and Wang, Z.L. (2016). Lawn Structured Triboelectric Nanogenerators for Scavenging Sweeping Wind Energy on Rooftops. *Adv. Mater.* 28, 1650–1656.
29. Zhao, K., Wang, Z.L., and Yang, Y. (2016). Self-Powered Wireless Smart Sensor Node Enabled by an Ultrastable, Highly Efficient, and Superhydrophobic-Surface-Based Triboelectric Nanogenerator. *ACS Nano* 10, 9044–9052.
30. Xie, Y., Wang, S., Lin, H., Jing, Q., Lin, Z., Niu, S., Wu, Z., and Wang, Z.L. (2013). Rotary Triboelectric Nanogenerator Based on a Hybridized Mechanism for Harvesting Wind Energy. *ACS Nano* 8, 7119–7125.
31. Li, W., Guo, H., Xi, Y., Wang, C., Javed, M.S., and Xia, X. (2017). Wgus sensor based on integrated wind-induced generating units for 360° wind energy harvesting and self-powered wind velocity sensing. *RSC Adv.* 7, 23208–23214.
32. Xi, L., Kun, Z., and Ya, Y. (2018). Effective polarization of ferroelectric materials by using a triboelectric nanogenerator to scavenge wind energy. *Nano Energy* 53, 622.
33. Hyeonseong, K., Zhou, Q., Daegyoun, K., and Il-Kwon, O.H. (2020). Flow-induced snap-through triboelectric nanogenerator. *Nano Energy* 68, 104379.
34. Guo, Y., Chen, Y., Ma, J., Zhu, H., Cao, X., and Wang, N. (2019). Harvesting wind energy: a hybridized design of pinwheel by coupling triboelectrification and electromagnetic induction effects. *Nano Energy* 60, 641–648.
35. Wang, Y., Wang, J., Xiao, X., Wang, S., Kien, P.T., Dong, J., Mi, J., Pan, X., Wang, H., and Xu, M. (2020). Multi-functional wind barrier based on triboelectric nanogenerator for power generation, self-powered wind speed sensing and highly efficient windshield. *Nano Energy* 73, 104736.
36. Wang, S., Mu, X., Wang, X., Gu, A.Y., Wang, Z.L., and Yang, Y. (2015). Elasto-aerodynamics-driven triboelectric nanogenerator for scavenging air-flow energy. *ACS Nano* 9, 9554–9563.
37. Zhang, H., Yang, Y., Zhong, X., Su, Y., Zhou, Y., Hu, C., and Wang, Z.L. (2014). Single-electrode-based rotating triboelectric nanogenerator for harvesting energy from tires. *ACS Nano* 8, 680–689.
38. Wang, S., Mu, X., Yang, Y., Sun, C., Gu, A.Y., and Wang, Z.L. (2015). Flow-driven triboelectric generator for directly powering a wireless sensor node. *Adv. Mater.* 27, 240–248.
39. Yang, Y., Zhang, H., Liu, R., Wen, X., Hou, T.C., and Wang, Z.L. (2013). Fully enclosed triboelectric nanogenerators for applications in water and harsh environments. *Adv. Energy Mater.* 3, 1563.
40. Yang, Y., Zhu, G., Zhang, H., Chen, J., Zhong, X., Lin, Z.H., Su, Y., Bai, P., Wen, X., and Wang, Z.L. (2013). Triboelectric nanogenerator for harvesting wind energy and as self-powered wind vector sensor system. *ACS Nano* 7, 9461–9468.
41. Wang, X., Wang, S., Yang, Y., and Wang, Z.L. (2015). Hybridized electromagnetic-trioboelectric nanogenerator for scavenging air-flow energy to sustainably power temperature sensors. *ACS Nano* 9, 4553–4562.

42. Zhao, Z., Pu, X., Du, C., Li, L., Jiang, C., Hu, W., and Wang, Z.L. (2016). Freestanding flag-type triboelectric nanogenerator for harvesting high-altitude wind energy from arbitrary directions. *ACS Nano* 10, 1780–1787.
43. Bae, J., Lee, J., Kim, S., Ha, J., Lee, B.S., Park, Y., Choong, C., Kim, J.B., Wang, Z.L., Kim, H.Y., et al. (2014). Flutter-driven triboelectrification for harvesting wind energy. *Nat. Commun.* 5, 4929.
44. Zhang, J., Childress, S., Libchaber, A., and Shelley, M. (2000). Flexible filaments in a flowing soap film as a model for one-dimensional flags in a two-dimensional wind. *Nature* 408, 835–839.
45. Zhu, L., and Peskin, C.S. (2003). Interaction of two flapping filaments in a flowing soap film. *Phys. Fluids* 15, 1954.
46. Kim, K., Baek, S.J., and Sung, H.J. (2002). An implicit velocity decoupling procedure for the incompressible navier–stokes equations. *Int. J. Numer. Methods Fluids* 38, 125.
47. Hwa Lee, J., Huang, W.X., and Jin Sung, H. (2014). Flapping dynamics of a flexible flag in a uniform flow. *Fluid Dyn. Res.* 46, 055517.
48. Jia, L., Li, F., and Yin, X. (2007). Coupling modes between two flapping filaments. *J. Fluid Mech.* 1, 199.
49. Ristroph, L., and Zhang, J. (2008). Anomalous hydrodynamic drafting of interacting flapping flags. *Phys. Rev. Lett.* 101, 194502.
50. Hübner, B., Walhorn, E., and Dinkler, D. (2004). A monolithic approach to fluid–structure interaction using space-time finite elements. *Comput. Methods Appl. Mech. Eng.* 193, 2087–2104.
51. Bathe, K.U.R., Zhang, H., and Ji, S. (1999). Finite element analysis of fluid flows fully coupled with structural interactions. *Comput. Struc.* 72, 1–16.
52. Zhang, X., Sessler, G., Ma, X., Xue, Y., and Wu, L. (2018). Broad bandwidth vibration energy harvester based on thermally stable wavy fluorinated ethylene propylene electret films with negative charges. *J. Micromech. Microeng.* 28, 065012. <https://iopscience.iop.org/article/10.1088/1361-6439/aab57d>
53. Fang, P., Zhang, X., and Ma, X. (2017). Flexible film-transducers based on polypropylene piezoelectrets: fabrication, properties, and applications in wearable devices. *Sens. Actuators A Phys.* 256, 35.
54. Fang, P., Ma, X., Li, X., Qiu, X., Gerhard, R., and Zhang, X. (2017). Fabrication, structure characterization, and performance testing of piezoelectret-film sensors for recording body motion. *IEEE Sens. J.* 18, 1558.
55. Anderson, J.D. (1984). *Fundamentals of aerodynamics* (McGraw-Hill).